

## Electronic Supplementary Information

### Experimental Section

**Materials:** CF was purchased from Shenzhen Green and Creative Environmental Science and Technology Co. Ltd. Sodium hydroxide (NaOH), ammonium chloride (NH<sub>4</sub>Cl), ethanol (C<sub>2</sub>H<sub>6</sub>O, 99.0%), salicylic acid (C<sub>7</sub>H<sub>6</sub>O<sub>3</sub>), sodium citrate dehydrate (C<sub>6</sub>H<sub>5</sub>Na<sub>3</sub>O<sub>7</sub>·2H<sub>2</sub>O), *p*-dimethylaminobenzaldehyde (C<sub>9</sub>H<sub>11</sub>NO), sodium hypophosphite (NaH<sub>2</sub>PO<sub>2</sub>), sodium nitroferricyanide dihydrate (C<sub>5</sub>FeN<sub>6</sub>Na<sub>2</sub>O·2H<sub>2</sub>O), sodium nitrite (NaNO<sub>2</sub>) sodium dihydrogen phosphate dihydrate (NaH<sub>2</sub>PO<sub>4</sub>), disodium hydrogen phosphate dodecahydrate (Na<sub>2</sub>HPO<sub>4</sub>) and sodium hypochlorite solution (NaClO) were purchased from Aladdin Ltd. (Shanghai, China). Nitric acid (HNO<sub>3</sub>), sulfuric acid (H<sub>2</sub>SO<sub>4</sub>), hydrogen peroxide (H<sub>2</sub>O<sub>2</sub>), hydrazine monohydrate (N<sub>2</sub>H<sub>4</sub>·H<sub>2</sub>O), phosphoric acid (H<sub>3</sub>PO<sub>4</sub>) and ethyl alcohol (C<sub>2</sub>H<sub>5</sub>OH) were purchased from Beijing Chemical Corp. (China). chemical Ltd. in Chengdu. The ultrapure water used throughout all experiments was purified through a Millipore system. All reagents were analytical reagent grade without further purification.

**Preparation of Cu(OH)<sub>2</sub> NA/CF:** CF was first cut into 0.5 cm × 1 cm pieces and cleaned by water and absolute ethanol before using. The CF was directly used as the working electrode to perform galvanostatic tests in 1.5 M NaOH aqueous solution for 20 min under 6 mA. After that, the CF was taken out and washed with distilled water and ethanol several times to obtain Cu(OH)<sub>2</sub> NA/CF, followed by drying at 60 °C.

**Preparation of Cu<sub>3</sub>P NA/CF:** To synthesize Cu<sub>3</sub>P NA/CF, the Cu(OH)<sub>2</sub> NA/CF was placed at the at the downstream side of the tube furnace and 20 mg NaH<sub>2</sub>PO<sub>2</sub> was put at the upstream side of the tube furnace. Then tube furnace was heated to 280°C with a heating rate of 2 °C min<sup>-1</sup> under an Ar atmosphere and held at this temperature for 120 min. After being naturally cooled to room temperature, Cu<sub>3</sub>P NA/CF was obtained.

**Characterizations:** Power XRD data were acquired by a LabX XRD-6100 X-ray diffractometer with a Cu Kα radiation (40 kV, 30 mA) of wavelength 0.154 nm (SHIMADZU, Japan). SEM images were collected on a GeminiSEM 300 scanning electron microscope (ZEISS, Germany) at an accelerating voltage of 5 kV. XPS measurements were performed on an ESCALABMK II X-ray photoelectron spectrometer using Mg as the exciting source. The absorbance data of spectrophotometer was measured on UV-Vis spectrophotometer. The ion chromatography data were collected on Metrohm 940 Professional IC Vario. ICP-MS analysis was performed on Thermo Fisher Scientific iCAP Q ICP-MS.

**Electrochemical measurements:** We used a H-type electrolytic cell (volume of the reaction cell: 50 mL for both anodic and cathodic compartment) separated by a Nafion 117 Membrane which was protonated by boiling in ultrapure water, H<sub>2</sub>O<sub>2</sub> (5%) aqueous solution and 0.5 M H<sub>2</sub>SO<sub>4</sub> at 80 °C for another 2 h, respectively. Both the anolyte and catholyte are 30 mL. A three-electrode configuration was utilized for electrochemical experiments using Cu<sub>3</sub>P NA/CF as the working electrode (0.5 × 0.5 cm<sup>2</sup>), Ag/AgCl (filled with saturated KCl solution) as the reference electrode and graphite rod (6 mm in diameter, 7.5 cm in length) as the counter electrode. The electrochemical experiments were carried out with an electrochemical workstation (CHI 660E) in 0.1 M PBS with 0.1 M NaNO<sub>2</sub>. The potentials reported in this work were converted to reversible hydrogen electrode (RHE) scale via calibration with the following equation: E (RHE) = E (vs. Ag/AgCl) + 0.61 V and the presented current density was normalized to the geometric surface area.

**Determination of NH<sub>4</sub><sup>+</sup>:** Owing to the large concentration of products, the obtained reaction solutions were diluted 100 times. Concentration of produced NH<sub>4</sub><sup>+</sup> was determined by spectrophotometry measurement with indophenol blue method.<sup>1</sup> In detail, 2 mL electrolyte was obtained from the cathodic chamber and mixed with 2 mL of a 1 M NaOH solution that contained salicylic acid and sodium citrate. Then, 1 mL of 0.05 M NaClO and 0.2 mL of 1 wt% C<sub>5</sub>FeN<sub>6</sub>Na<sub>2</sub>O. After standing at room temperature for 2 h, the ultraviolet-visible absorption spectrum was measured. The concentration of NH<sub>4</sub><sup>+</sup> was determined using the absorbance at a wavelength of 655 nm. The concentration-absorbance curve was calibrated using standard NH<sub>4</sub><sup>+</sup> solution with a series of concentrations. The fitting curve ( $y = 437x + 0.0397$ ,  $R^2 = 0.999$ ) shows good linear relation of absorbance value with NH<sub>4</sub><sup>+</sup> concentration.

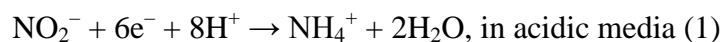
**Determination of NO<sub>2</sub><sup>-</sup>:** Owing to the large concentration of solution, the obtained reaction solutions were diluted 1000 times. The NO<sub>2</sub><sup>-</sup> concentration was analyzed using the Griess test.<sup>2</sup> The Griess reagent was prepared by dissolving 0.1 g of N-(1-naphthyl)ethyldiamine dihydrochloride, 1.0 g of sulfonamide and 2.94 mL of H<sub>3</sub>PO<sub>4</sub> in 50 mL of deionized H<sub>2</sub>O. In a typical colorimetric assay, the Griess reagent (1.0 mL) was mixed with the nitrite-containing solution (1.0 mL) and H<sub>2</sub>O (2.0 mL), and allowed to react at room temperature for 10 min, in which the sulfonamide reacts with the NO<sub>2</sub><sup>-</sup> to form a diazonium salt and then further reacts with the amine to form an azo dye (magenta). The absorbance at 540 nm was measured by ultraviolet-visible spectroscopy and the NO<sub>2</sub><sup>-</sup> concentration was calculated ( $y = 0.181x + 0.0535$ ,  $R^2 = 0.999$ ).

**Determination of N<sub>2</sub>H<sub>4</sub>:** The N<sub>2</sub>H<sub>4</sub> production was estimated by the method of Watt and Chrisp.<sup>3</sup> The color reagent was a mixed solution of 5.99 g C<sub>9</sub>H<sub>11</sub>NO, 30 mL HCl and 300 mL

C<sub>2</sub>H<sub>5</sub>OH. In detail, 5 mL electrolyte was removed from the electrochemical reaction vessel, and added into 5 mL prepared color reagent and stirred 15 min at 25 °C. The absorbance of such solution at the absorbance of 455 nm was measured to quantify the hydrazine yields with a standard curve of hydrazine ( $y = 0.0479 x + 0.0041$ ,  $R^2 = 0.999$ ).

#### Determination of FE and NH<sub>4</sub><sup>+</sup> yield:

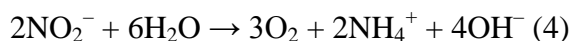
Equations of cathode reaction of NO<sub>2</sub><sup>-</sup>RR:



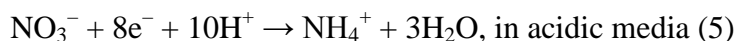
Equations of anode reaction:



Possible overall reaction:



Equations of cathode reaction of NO<sub>3</sub><sup>-</sup>RR:



FE toward NH<sub>4</sub><sup>+</sup> via NO<sub>2</sub><sup>-</sup>RR was calculated by equation:

$$\text{FE} = 6 \times F \times ([\text{NH}_4^+] \times V / M_{\text{NH}_4^+}) / Q \times 100\% \text{ (7)}$$

FE toward NH<sub>4</sub><sup>+</sup> via NO<sub>3</sub><sup>-</sup> reduction reaction (NO<sub>3</sub><sup>-</sup>RR) was calculated by equation:

$$\text{FE} = 8 \times F \times ([\text{NH}_4^+] \times V / M_{\text{NH}_4^+}) / Q \times 100\% \text{ (8)}$$

NH<sub>4</sub><sup>+</sup> yield rate was calculated using the following equation:

$$\text{NH}_4^+ \text{ yield rate} = [\text{NH}_4^+] \times V / (M_{\text{NH}_4^+} \times t \times A) \text{ (9)}$$

For the NO<sub>2</sub><sup>-</sup> electroreduction experiments, the selectivity of NH<sub>4</sub><sup>+</sup> is acquired by equation:

$$\text{Selectivity} = [\text{NH}_4^+] / \Delta[\text{NO}_2^-] \times 100\% \text{ (10)}$$

Conversion rate:

$$\text{Conversion rate} = \Delta[\text{NO}_2^-] / [\text{NO}_2^-] \times 100\% \text{ (11)}$$

Where 6 and 8 are electron transfer numbers for NO<sub>2</sub><sup>-</sup>RR and NO<sub>3</sub><sup>-</sup>RR, respectively (the reduction of NO<sub>2</sub><sup>-</sup> to NH<sub>4</sub><sup>+</sup> consumes 6 electrons, and the reduction of NO<sub>3</sub><sup>-</sup> to NH<sub>4</sub><sup>+</sup> consumes 8 electrons), F is the Faradic constant (96500 C mol<sup>-1</sup>), M<sub>NH<sub>4</sub><sup>+</sup></sub> is the molar mass of NH<sub>4</sub><sup>+</sup> (= 18), [NH<sub>4</sub><sup>+</sup>] is the measured NH<sub>4</sub><sup>+</sup> concentration (The unit of [NH<sub>4</sub><sup>+</sup>] is mg L<sup>-1</sup>), [NO<sub>2</sub><sup>-</sup>] is the initial concentration of NO<sub>2</sub><sup>-</sup> (The unit of [NO<sub>2</sub><sup>-</sup>] is mg L<sup>-1</sup>), Δ[NO<sub>2</sub><sup>-</sup>] is the converted NO<sub>2</sub><sup>-</sup> concentration (the concentration difference of NO<sub>2</sub><sup>-</sup> before and after electrolysis), V is the volume of electrolyte in the cathodic or anodic compartment (30 mL),

the unit of  $V$  is L,  $Q$  is the total quantity of applied electricity;  $t$  is the reduction time (2 h),  $A$  is the geometric area of working electrode ( $0.5 \times 0.5 \text{ cm}^2$ ), and  $[\text{NO}_2^-]$  is the concentration difference of  $\text{NO}_2^-$  before and after electrolysis. Besides,  $E^0$  (the redox potential of  $\text{NO}_2^-/\text{NH}_3$  ( $\text{NH}_4^+$ ) = 0.897 V vs. NHE.

### Computational details

First-principles calculations were performed using Vienna ab initio simulation package (VASP) within the framework of density functional theory (DFT).<sup>4</sup> The projected augmented wave (PAW) pseudopotential<sup>5</sup> with the Perdew, Burke, and Ernzerhof (PBE) functional<sup>6</sup> were adopted. The DFT+D3 method was used to describe the long-range dispersion interaction.<sup>7</sup> The convergence criteria for the total energy and the force are  $10^{-5}$  eV and  $0.02 \text{ eV}\text{\AA}^{-1}$ , respectively. Spin polarization was considered for all the calculations. The charge transfer was calculated using Bader analysis.<sup>8</sup> To simulate the surface, the slab model has been used with a vacuum layer of at least  $16 \text{ \AA}$ . The Monkhorst-Pack (MP) grid<sup>9</sup> was used to sample the Brillouin zone with the kinetic cutoff energy of 450 eV for the plane-wave basis set. For modelling the unit cell of the  $\text{Cu}_3\text{P}$  bulk, the  $6 \times 6 \times 5$  MP grid was used, and for the surface unit cell and supercell the  $5 \times 5 \times 1$  and  $3 \times 3 \times 1$  MP grids were adopted, respectively.

With the above settings, as shown in Fig. S17a, the calculated lattice parameters of the  $\text{Cu}_3\text{P}$  bulk ( $a = 6.86 \text{ \AA}$  and  $c = 7.08 \text{ \AA}$ ) are in good agreement with previous works.<sup>10</sup> The  $\text{Cu}_3\text{P}(300)$  surfaces were adopted to study the mechanism of the nitrite reduction reaction. It is noted that there are three different terminations for the  $\text{Cu}_3\text{P}(300)$  surface, as shown in Fig. S18. The three slab models contain six atomic layers, in which the bottom three layers are fixed to mimic the bulk. To determine the most stable one, we calculated and compared the surface energy ( $\gamma$ ) of the three surfaces according to the equation:

$$\gamma = \frac{1}{2A} [E_{slab}^{unrelax} - nE_{bulk}] + \frac{1}{A} [E_{slab}^{relax} - E_{slab}^{unrelax}]$$

where,  $A$  is the surface area of one side of the slab;  $n$  is the number of  $\text{Cu}_3\text{P}$  units of the slab;  $E_{bulk}$  is the total energy of the bulk  $\text{Cu}_3\text{P}$  formula unit;  $E_{slab}^{relax}$  and  $E_{slab}^{unrelax}$  are the total energies of the relaxed and unrelaxed slabs, respectively. The calculations indicate that the most stable one has a surface energy of  $1.403 \text{ J/m}^2$  (the one presented in Fig. S18a). Then the  $\text{NO}_2^-$ RR was studied over the  $\text{Cu}_3\text{P}(300)$  ( $\sqrt{2} \times \sqrt{2}$ ) supercell as shown in Fig. S19, which is constructed based on the structure in Fig. S18a.

To calculate the change in Gibbs free energy for the elemental steps, the computational hydrogen electrode (CHE) model has been adopted,<sup>11</sup> using the following equation:

$$\Delta G = \Delta E + \Delta E_{\text{ZPE}} - T\Delta S + \Delta G_{\text{U}}$$

In the equation, the total energy ( $E$ ), zero-point energy ( $E_{\text{ZPE}}$ ), and entropy ( $S$ ) of the intermediates were obtained from DFT calculations (Table S4 and S5), while the thermodynamic corrections of the free molecules taken from the NIST databases.<sup>12</sup> In addition,  $\Delta G_{\text{U}}$  is the free-energy contributions related to the applied electrode potential  $U$ , which was used to ensure that every step in the assumed NRR procedures is exergonic. When calculating the adsorption energy of  $\text{NO}_2^-$ , the neutral  $\text{HNO}_2$  in gas phase was chosen as reference and then the energy of  $\text{NO}_2^-$  was obtained from the thermodynamic cycle to avoid the difficulty of using periodic DFT for the charged system.<sup>13</sup>

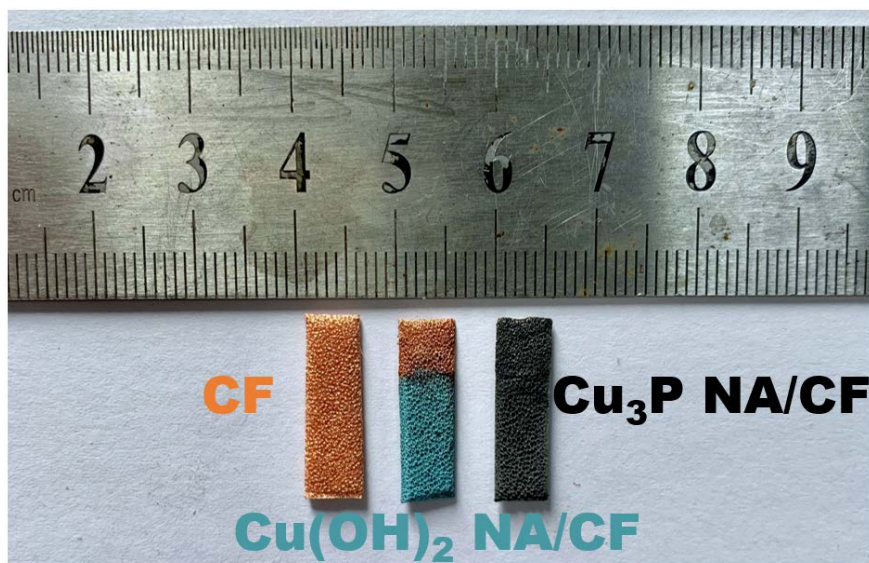


**Fig. S1.** Photograph of bare CF (left),  $\text{Cu(OH)}_2$  NA/CF (middle), and  $\text{Cu}_3\text{P}$  NA/CF (right).

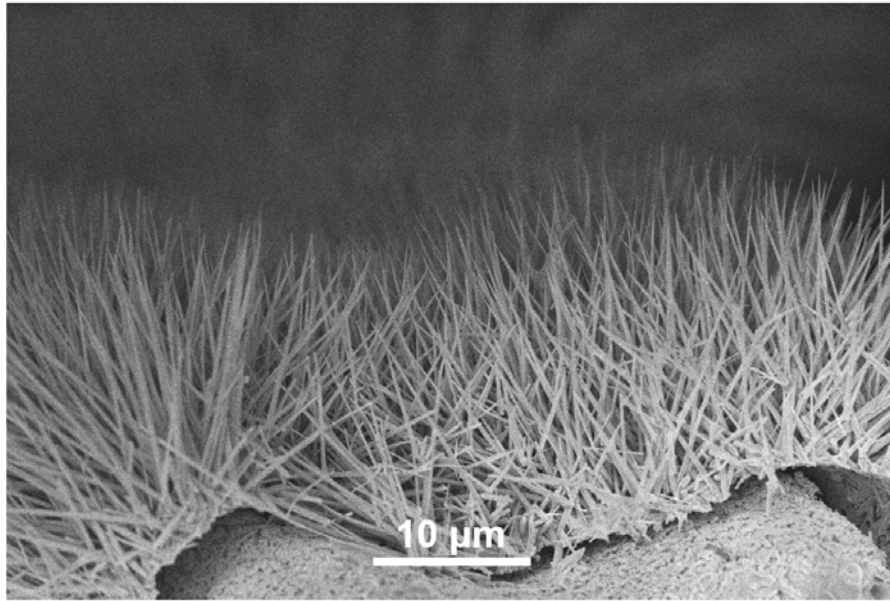


**Fig. S2.** Side-view SEM image of  $\text{Cu}_3\text{P}$  NA/CF.

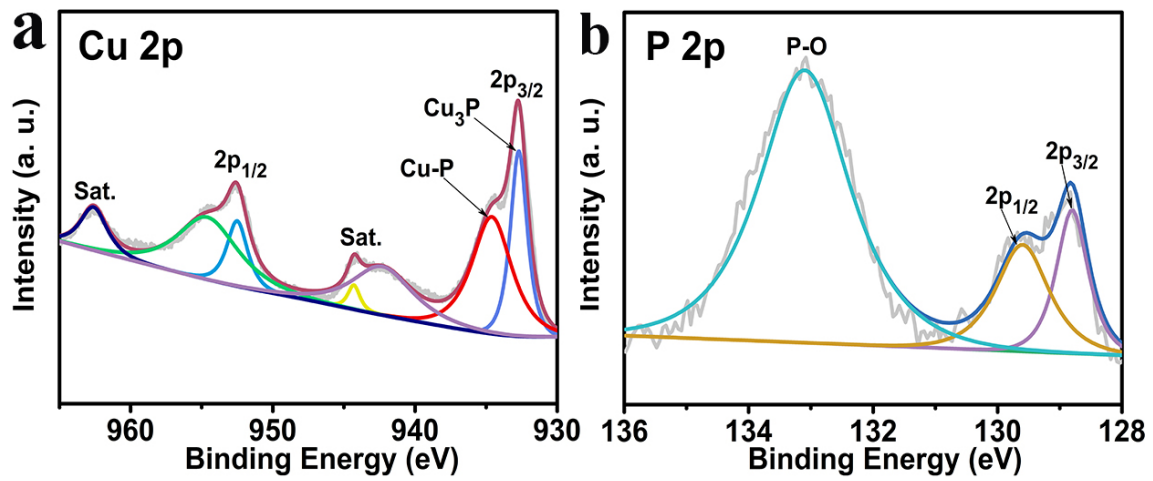
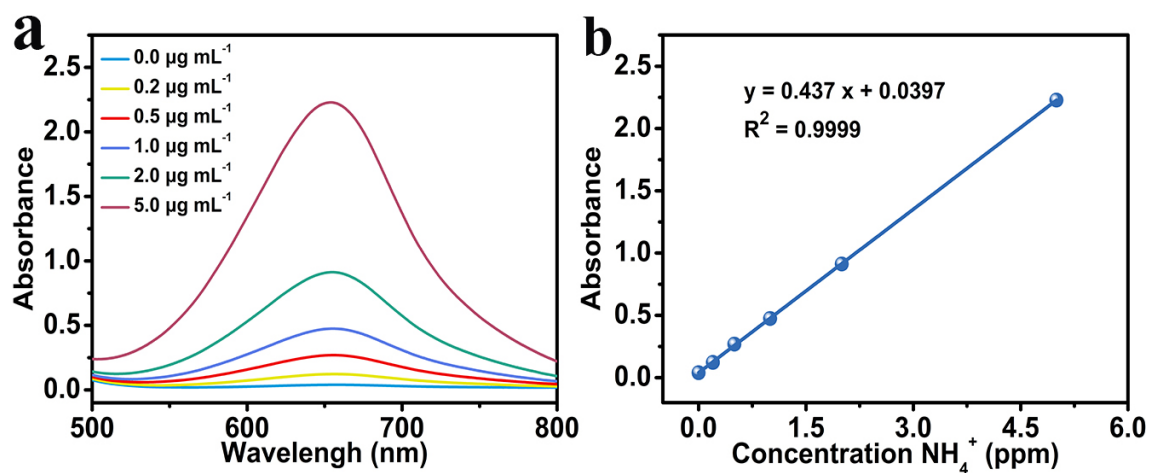
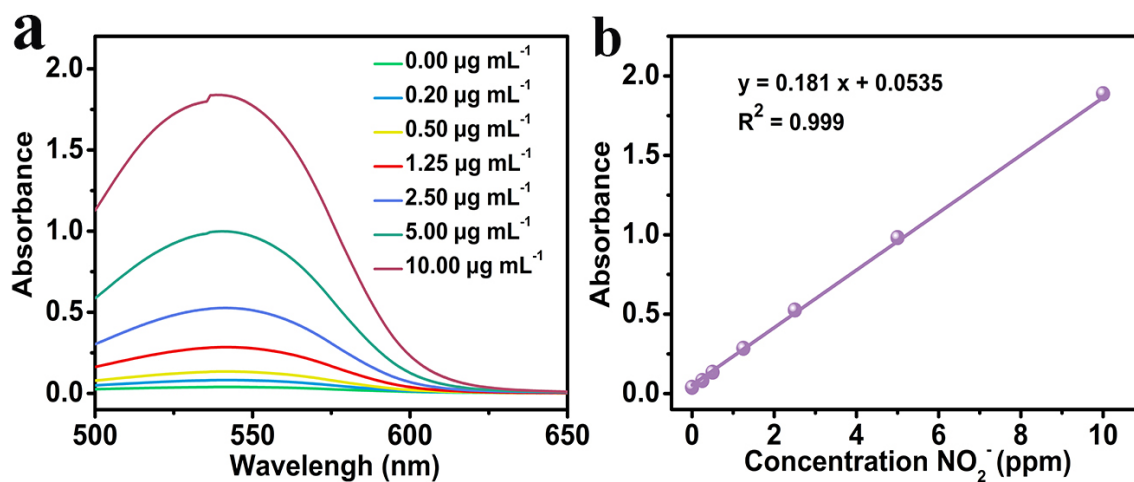


Fig. S3. XPS spectra of Cu<sub>3</sub>P NA/CF in the (a) Cu 2p and (b) P 2p regions.



**Fig. S4.** (a) UV-Vis absorption curves of indophenol assays kept with different concentrations of  $\text{NH}_4^+$  for 2 h at room temperature. (b) Calibration curve used to estimate the concentration of  $\text{NH}_4^+$  concentration.



**Fig. S5.** (a) UV-Vis curves of various  $\text{NO}_2^-$  concentrations after incubated for 10 min at room temperature. (b) Calibration curve used for calculation of  $\text{NO}_2^-$  concentrations.

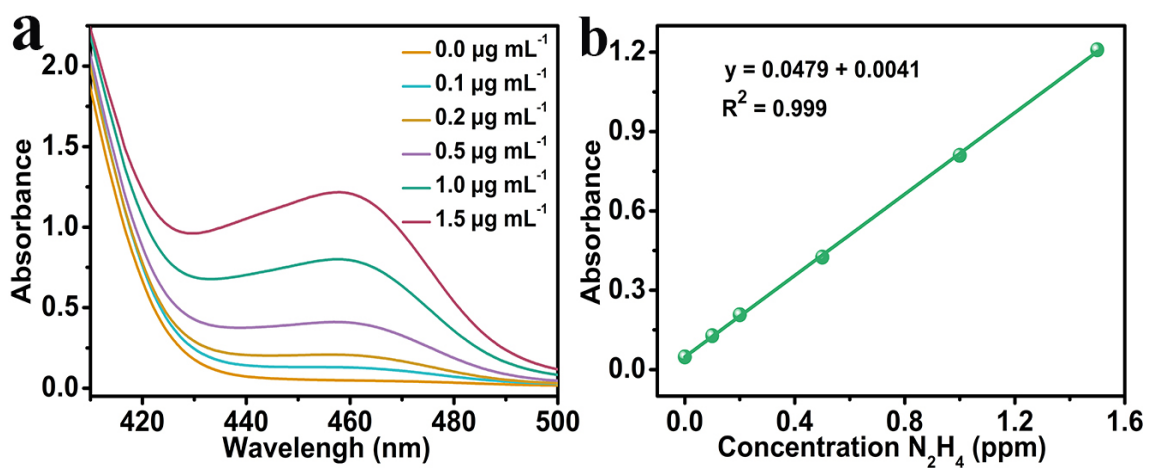


**Fig. S6.** (a) UV-Vis absorption spectra of various  $\text{N}_2\text{H}_4$  concentrations stained with the  $\text{C}_9\text{H}_{11}\text{NO}$  indicator after incubated for 15 min at room temperature. (b) Calibration curve used for calculation of  $\text{N}_2\text{H}_4$  concentration.

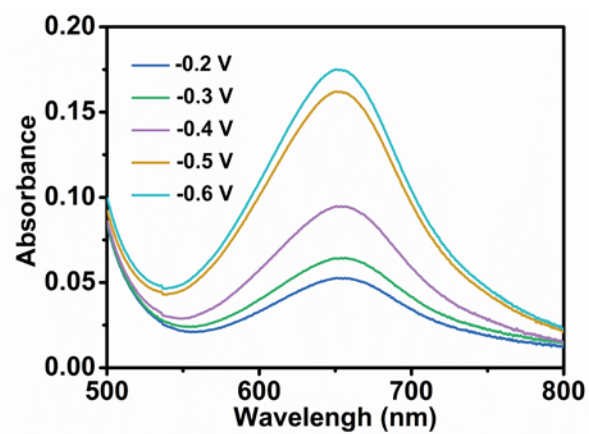


**Fig. S7.** UV-Vis absorption spectra of the electrolytes stained with the indophenol indicator after bulk electrolysis for 2 h.

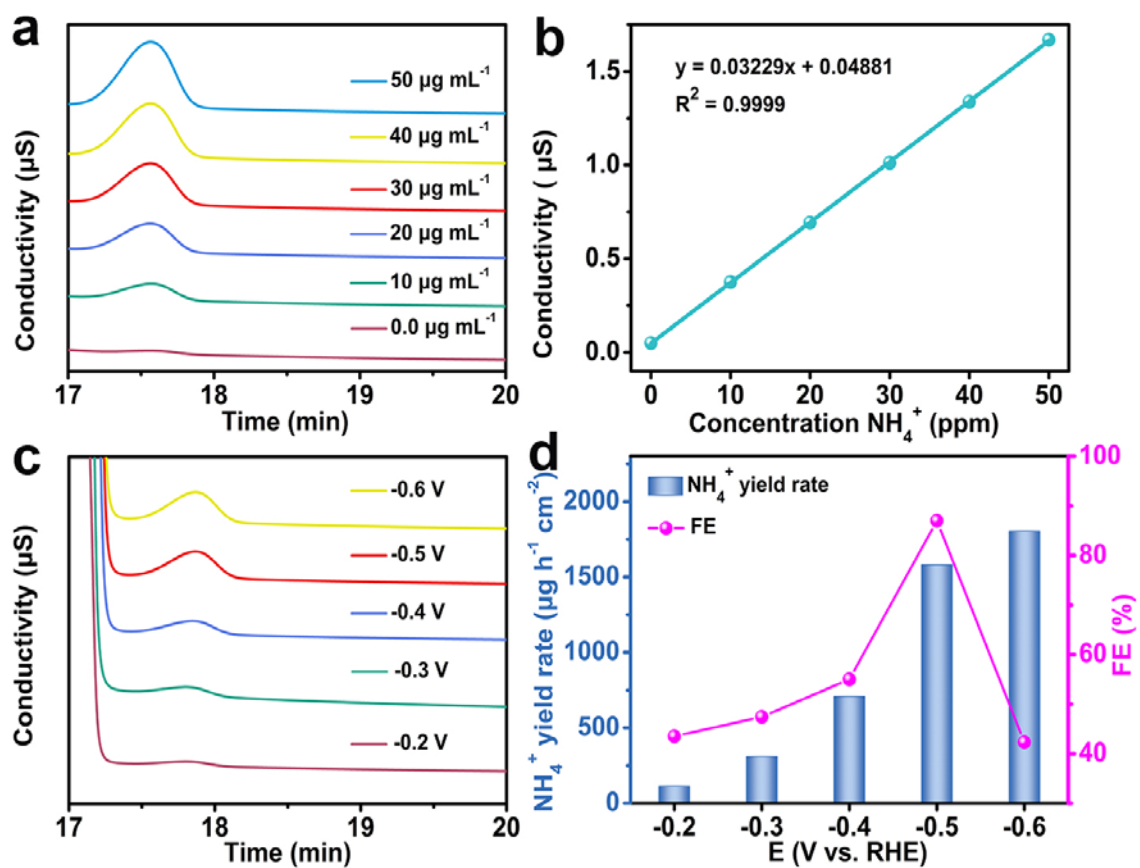


**Fig. S8.** (a) Ion chromatograms of  $\text{NH}_4\text{Cl}$  with different concentrations in 0.1 M PBS and (b) corresponding standard curve. (c) Ion chromatograms for the electrolytes at a series of potentials after electrolysis for 2 h. (d) Ammonium yield rates and FEs of  $\text{Cu}_3\text{P NA/CF}$  at corresponding potential.

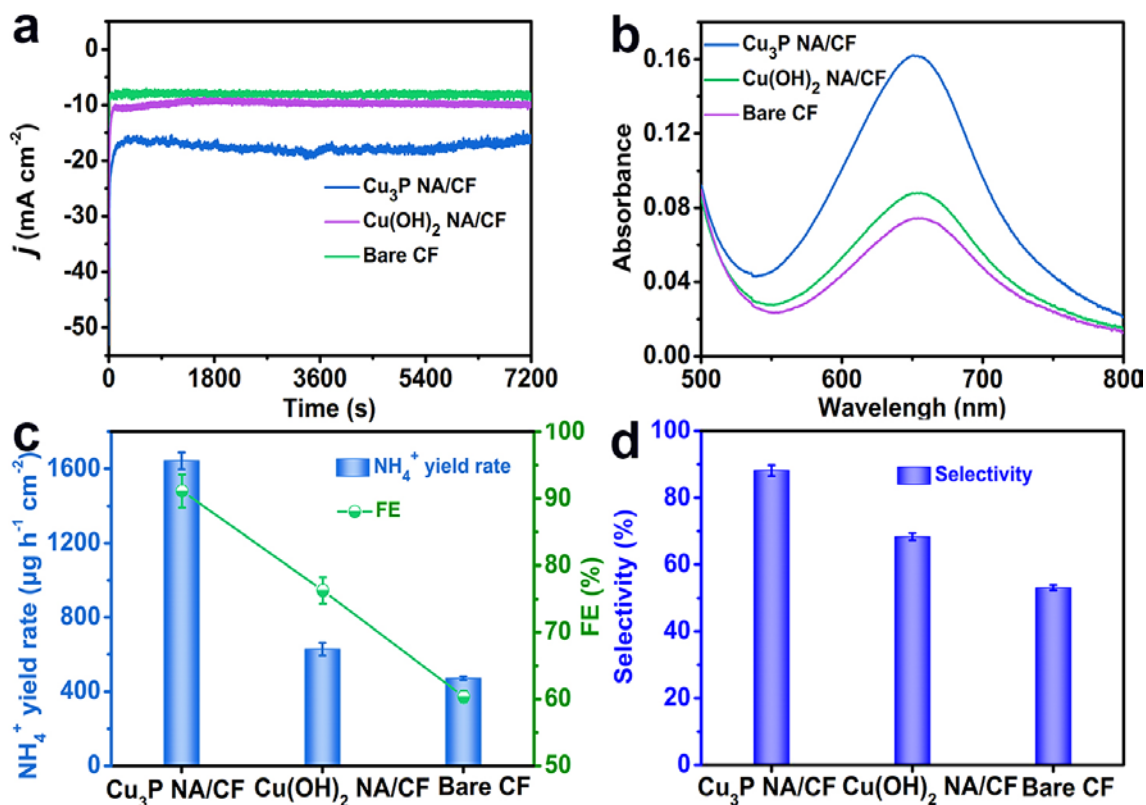


**Fig. S9.** (a) Chronoamperometry curves of Cu<sub>3</sub>P NA/CF, Cu(OH)<sub>2</sub> NA/CF, and bare CF substrate at -0.5 V vs. RHE in 0.1 M PBS with 0.1 M NaNO<sub>2</sub>. (b) UV-Vis absorption spectra of the electrolytes stained with the indophenol indicator after bulk electrolysis for 2 h. (c) Corresponding ammonium yield rates and FEs of Cu<sub>3</sub>P NA/CF, Cu(OH)<sub>2</sub> NA/CF and bare CF substrate. (d) Corresponding selectivity toward ammonium of Cu<sub>3</sub>P NA/CF, Cu(OH)<sub>2</sub> NA/CF and bare CF substrate.

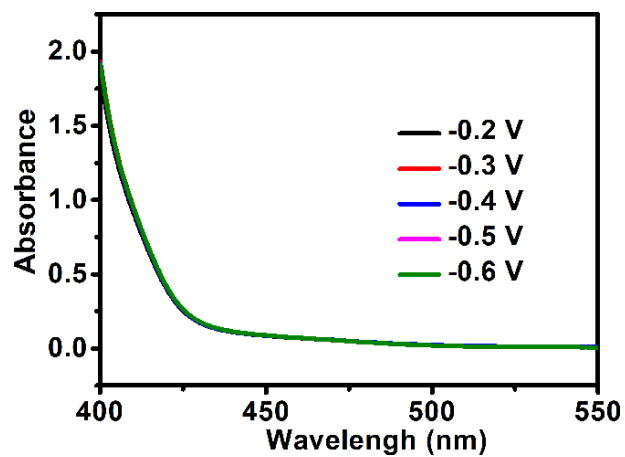


**Fig. S10.** UV-Vis absorption spectra of the electrolytes estimated by the method of Watt and Chrisp after 2 h electrolysis at each given potential under ambient conditions.



**Fig. S11.** The reaction between NaNO<sub>2</sub> and acids (such as diluted hydrochloric acid (0.1 M HCl) solution) can produce undesired nitric oxide (NO), nitrogen dioxide (NO<sub>2</sub>) contaminants.

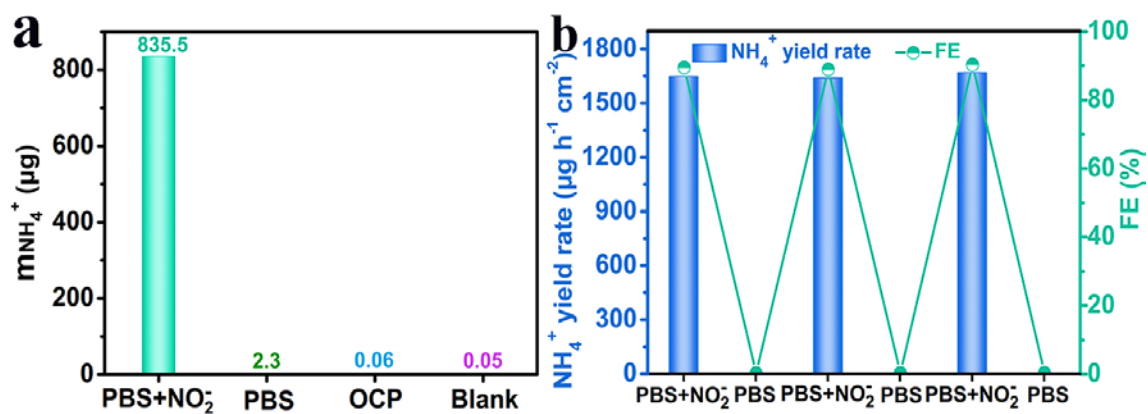


**Fig. S12.** (a) Amounts of produced ammonium comparison under different conditions. (b) Ammonium yield rates and FEs of Cu<sub>3</sub>P NA/CF during the alternating cycle test between NO<sub>2</sub><sup>-</sup>-containing and NO<sub>2</sub><sup>-</sup>-free 0.1 M PBS solution.

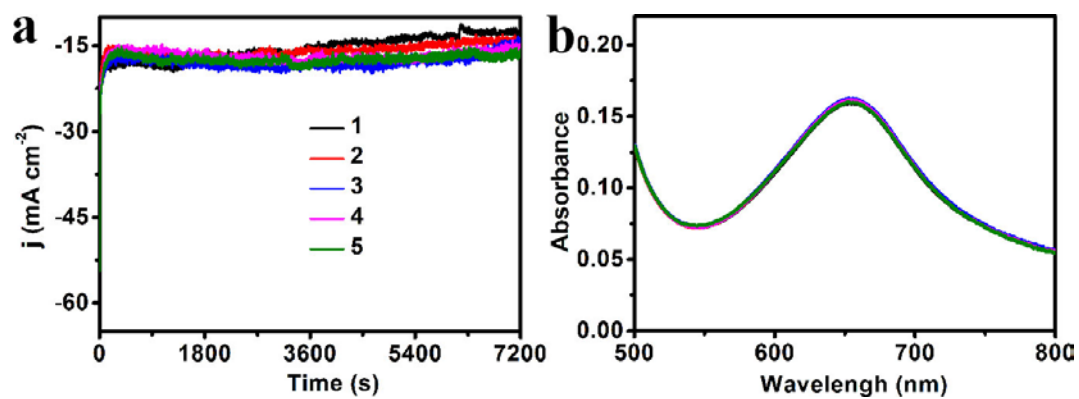


**Fig. S13.** (a) Chronoamperometry curves of Cu<sub>3</sub>P NA/CF under recycling tests for NO<sub>2</sub><sup>-</sup>RR at -0.5 V vs. RHE in 0.1 M PBS with 0.1 M NaNO<sub>2</sub>. (b) UV-Vis absorption spectra of the electrolytes stained with indophenol indicator after NO<sub>2</sub><sup>-</sup>RR electrolysis.

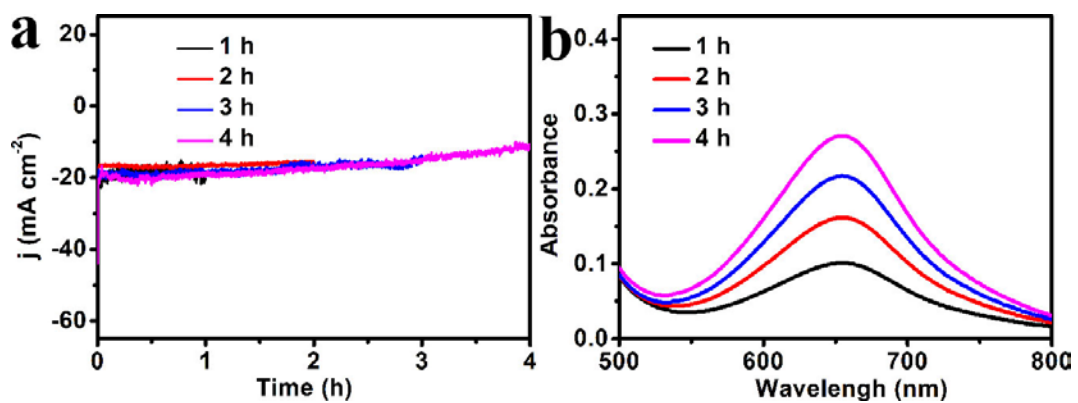


**Fig. S14.** (a) Chronoamperometry curves under different time periods. (b) UV-Vis absorption spectra of the electrolytes stained with indophenol indicator after  $\text{NO}_2^-$  RR electrolysis.

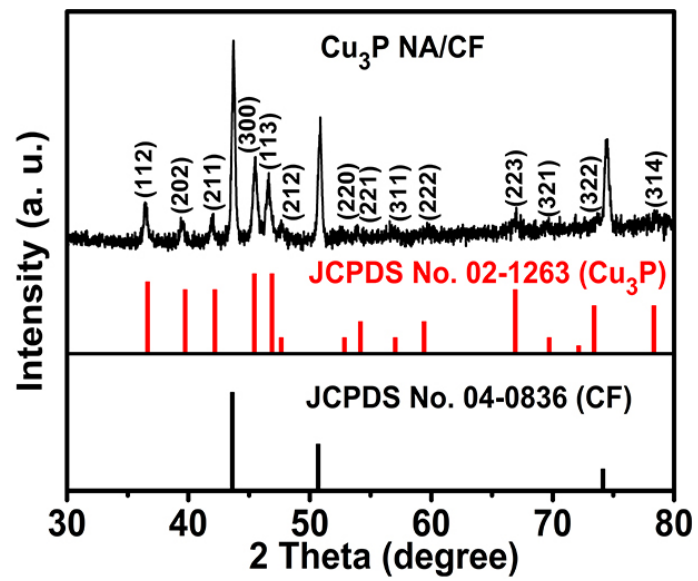


**Fig. S15.** XRD pattern of Cu<sub>3</sub>P NA/CF after stability tests.

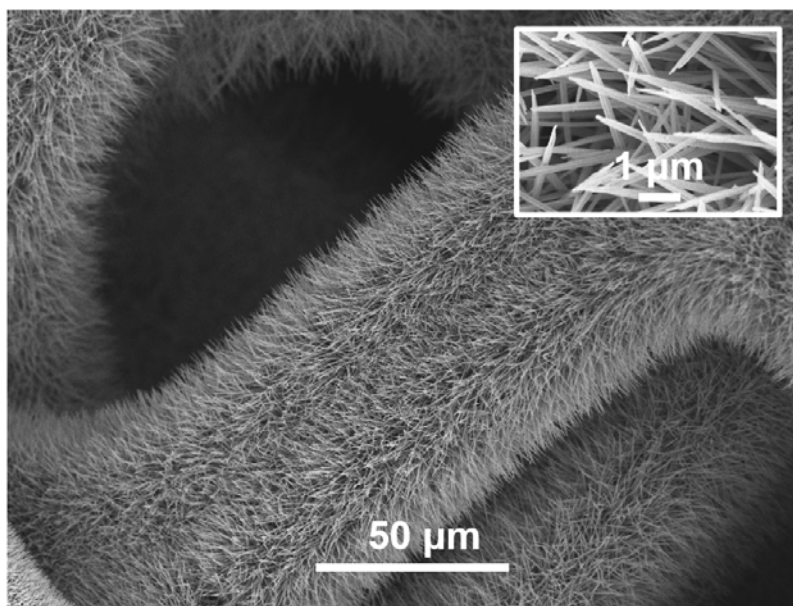


**Fig. S16.** SEM images of Cu<sub>3</sub>P NA/CF after stability tests.

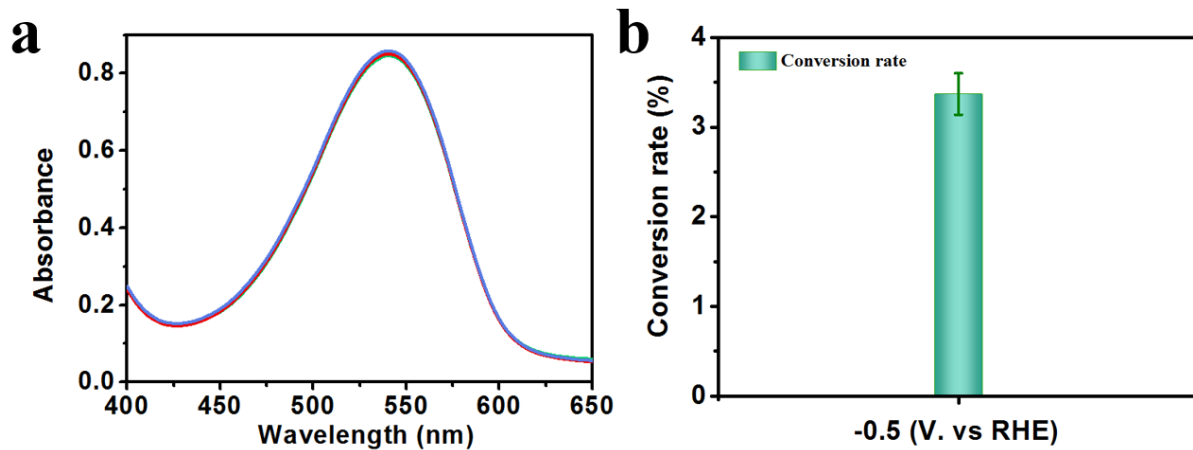


**Figure S17.** (a) UV-Vis absorption spectra of the electrolyte solutions after long-term electrolysis (10 h) colored with Griess reagent and corresponding (b) conversion rate of  $\text{NO}_2^-$ .

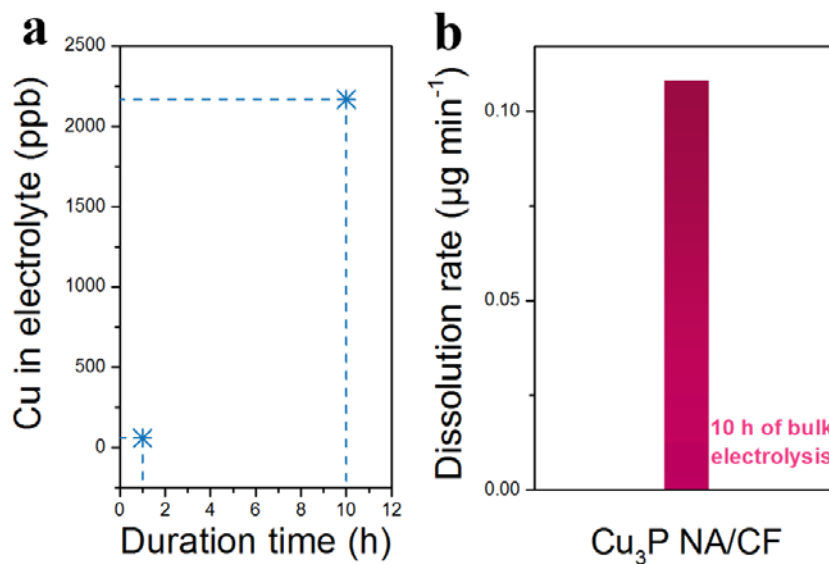


**Fig. S18.** (a) ICP-MS data characterizing the time-dependent concentrations of Cu dissolved (catalyst loss of Cu<sub>3</sub>P NA/CF) in 30 ml of electrolyte as the NO<sub>2</sub><sup>-</sup>RR electrocatalysis proceeds. (b) Dissolution rate of Cu<sub>3</sub>P NA/CF during the long-term bulk NO<sub>2</sub><sup>-</sup>RR electrolysis tests at -0.5 V vs. RHE in 0.1 M PBS with 0.1 M NaNO<sub>2</sub>.

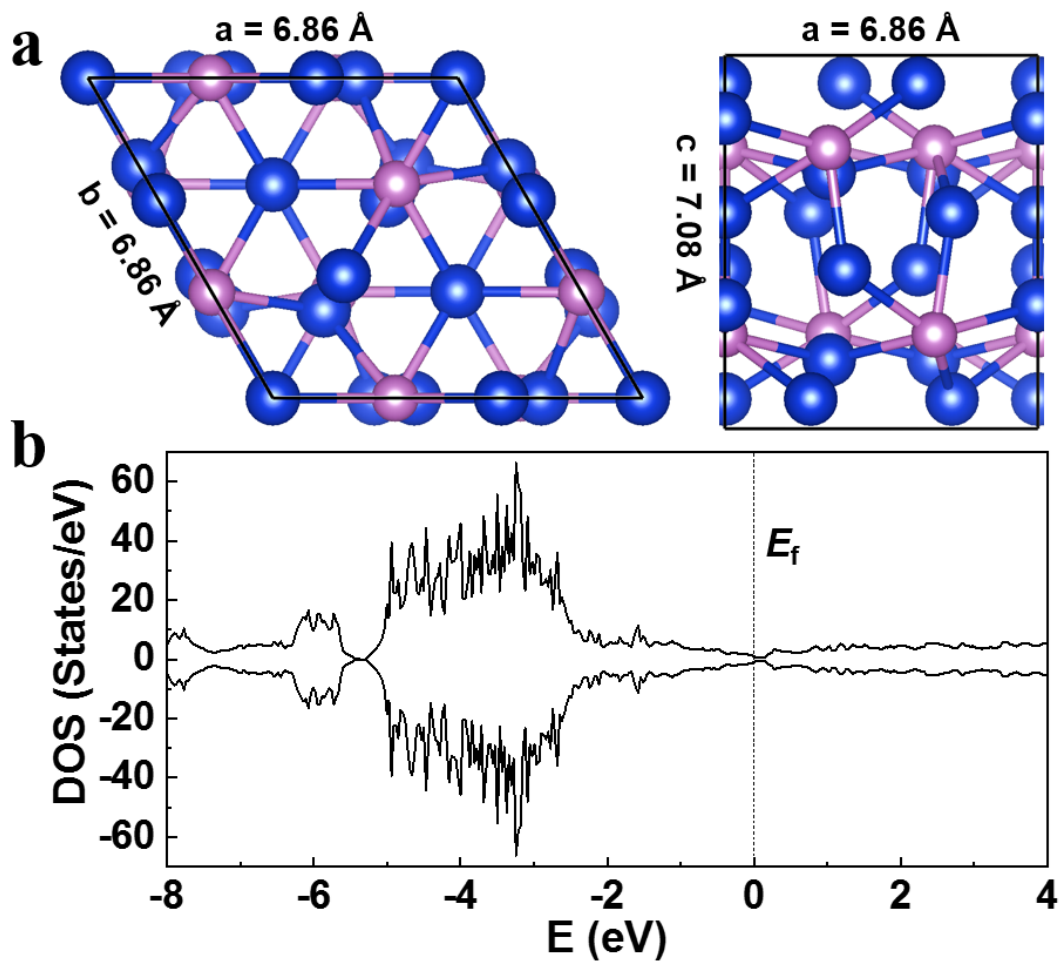


**Fig. S19.** (a) The unit cell together with the theoretical lattice parameters and (b) the total densities of states (DOS) of the Cu<sub>3</sub>P bulk. The dashed line in (b) denotes the position of the Fermi level ( $E_f$ ). Blue and light purple spheres represent Cu and P atoms, respectively.

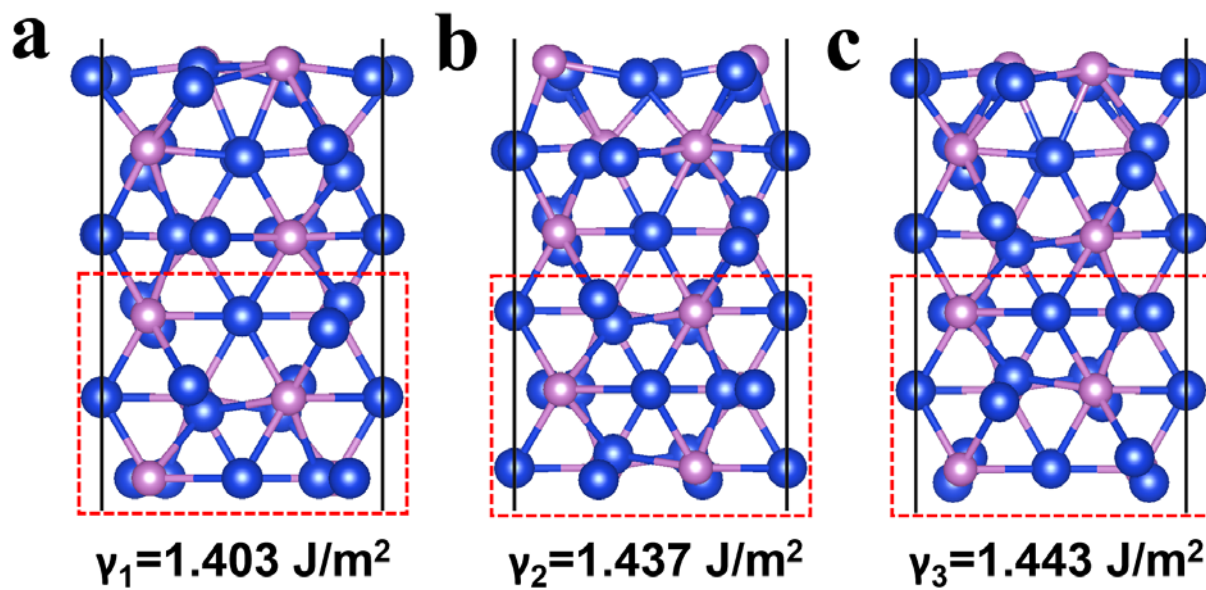


**Fig. S20.** The side views of the slab models of the  $\text{Cu}_3\text{P}(300)$  unit cell with three different terminations. The models contain six atomic layers, in which the bottom three layers enclosed by the dashed red lines are fixed to mimic the bulk. The surface energies ( $\gamma$ ) for the three surfaces are given.

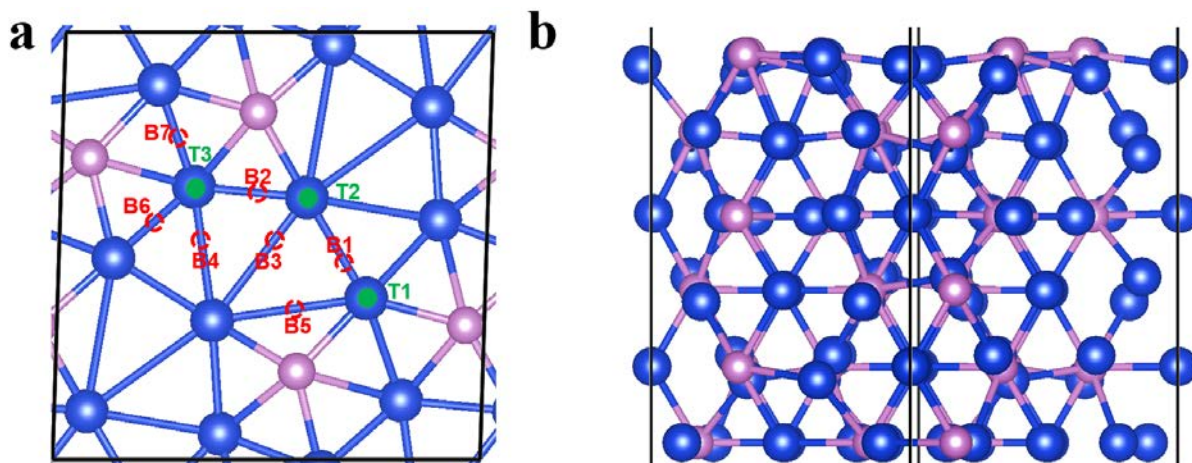


**Fig. S21.** (a). The top (a) and side (b) views of the  $\text{Cu}_3\text{P}(300)$  ( $\sqrt{2} \times \sqrt{2}$ ) supercell (the one with the lowest surface energy as shown in Fig. S18a). The adsorption sites for  $\text{NO}_2^-$  are marked in (a).

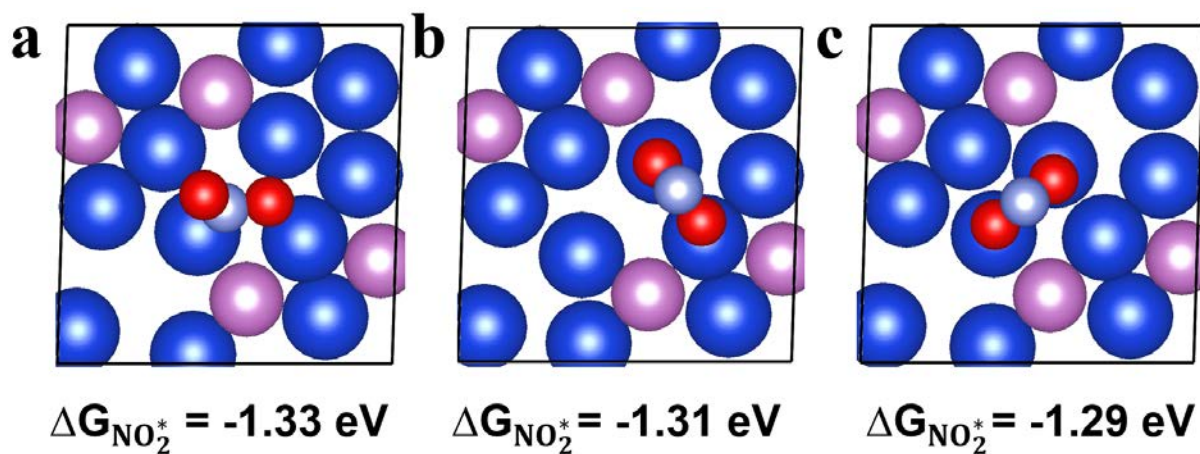


**Fig. S22.** The atomic structures together with the adsorption free energies for the three configurations with higher stability are given for  $\text{NO}_2^-$  adsorption on the  $\text{Cu}_3\text{P}(300)$  surface. Blue, light purple, grey, and red spheres represent Cu, P, N, and O atoms, respectively. The systems in (a) and (b) are further studied for the nitrite reduction reaction.

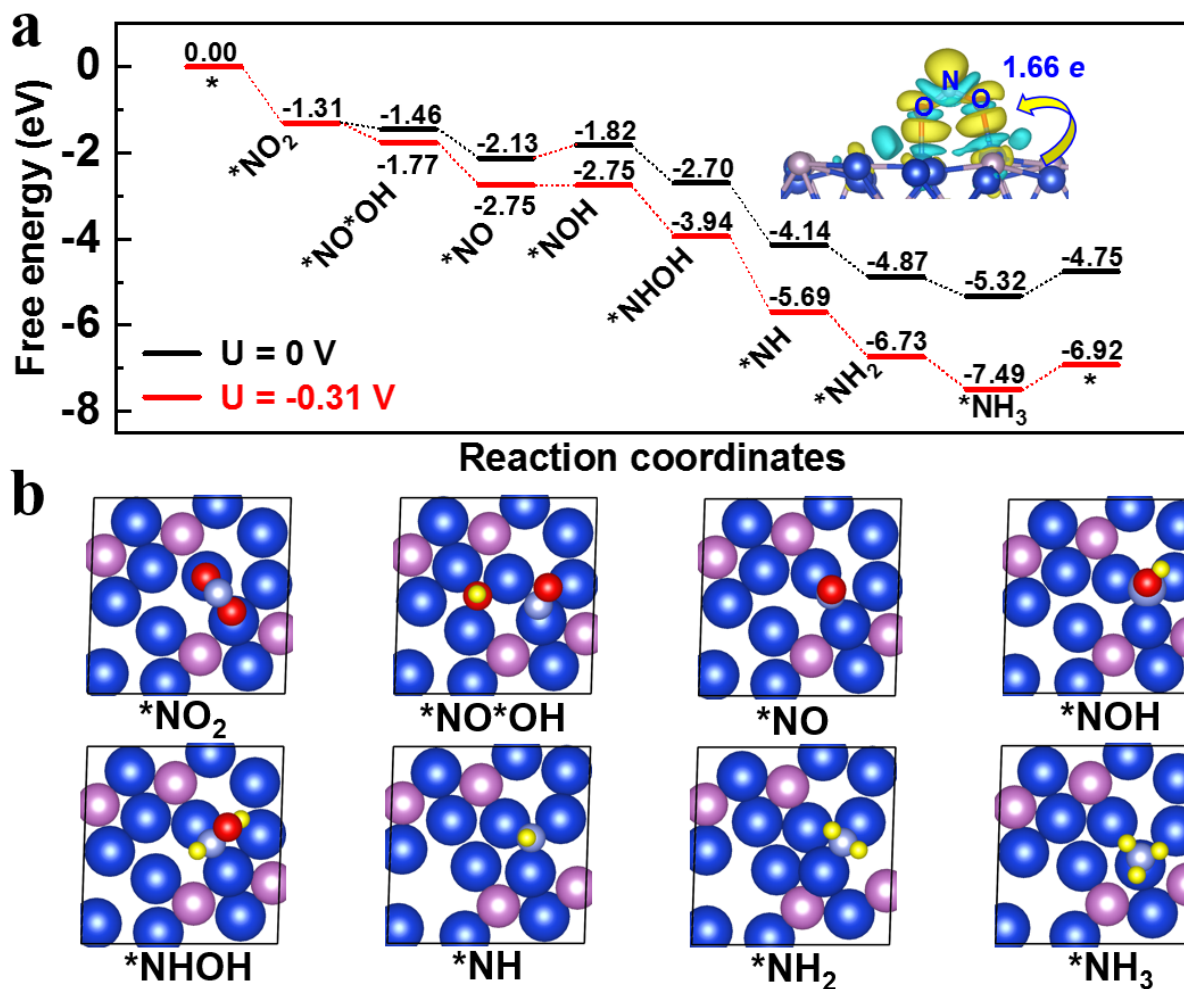
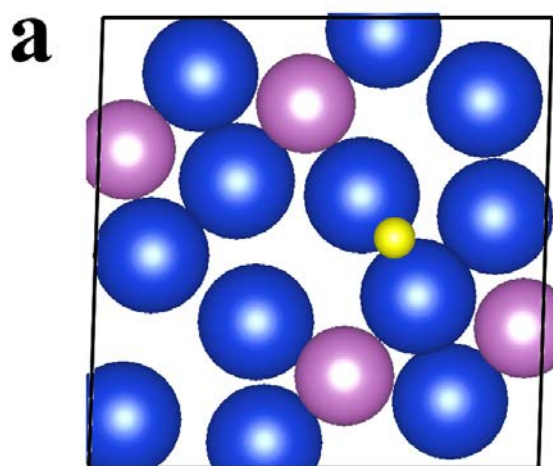
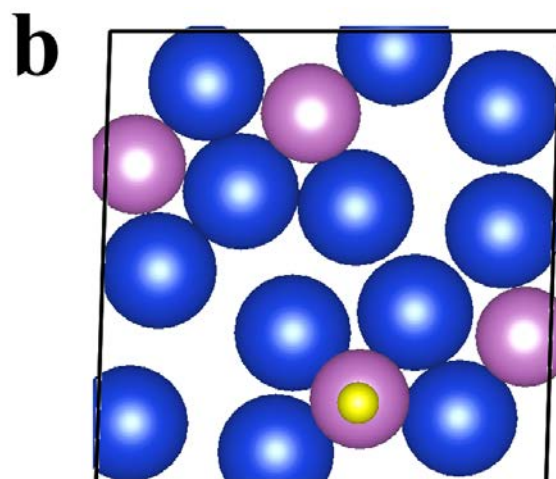


**Fig. S23.** (a) Free energy diagrams at different applied potentials for the nitrite reduction process on the  $\text{Cu}_3\text{P}(300)$  surface, starting with the  $\text{NO}_2^-$  adsorbed at B1 site as shown in Fig. S19. (b) Atomic structures of the corresponding intermediates. In (a), the charge density difference for the adsorbed  $\text{NO}_2^-$  is presented as an inset, where yellow and green regions denote electron accumulation and loss, respectively. The positions of the N and O atoms are roughly marked.



$$\Delta G_{\text{H}^*} = 0.00 \text{ eV}$$



$$\Delta G_{\text{H}^*} = 0.34 \text{ eV}$$

**Fig. S24.** The atomic structures together with the adsorption free energies for the atomic H adsorption on the  $\text{Cu}_3\text{P}(300)$  surface at B1 (a) and B5 (b) sites.

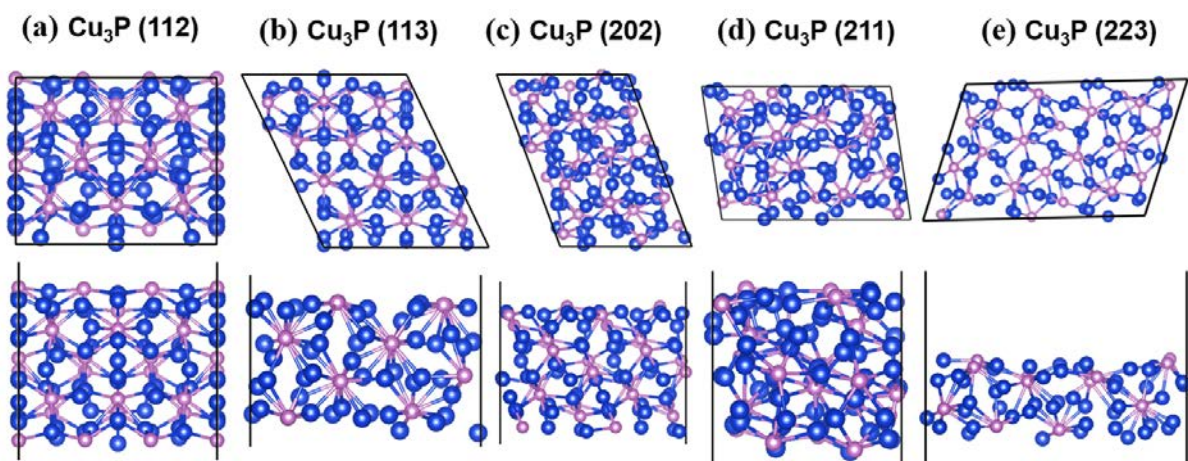


**Fig. S25.** The top (a) and side (b) views of the  $\text{Cu}_3\text{P}$ (112) ( $1\times 1$ ), (113) ( $1\times 1$ ), (202) ( $1\times 2$ ), (211) ( $1\times 1$ ), and (223) ( $1\times 1$ ) surfaces. Blue and light purple spheres represent Cu and P atoms, respectively.

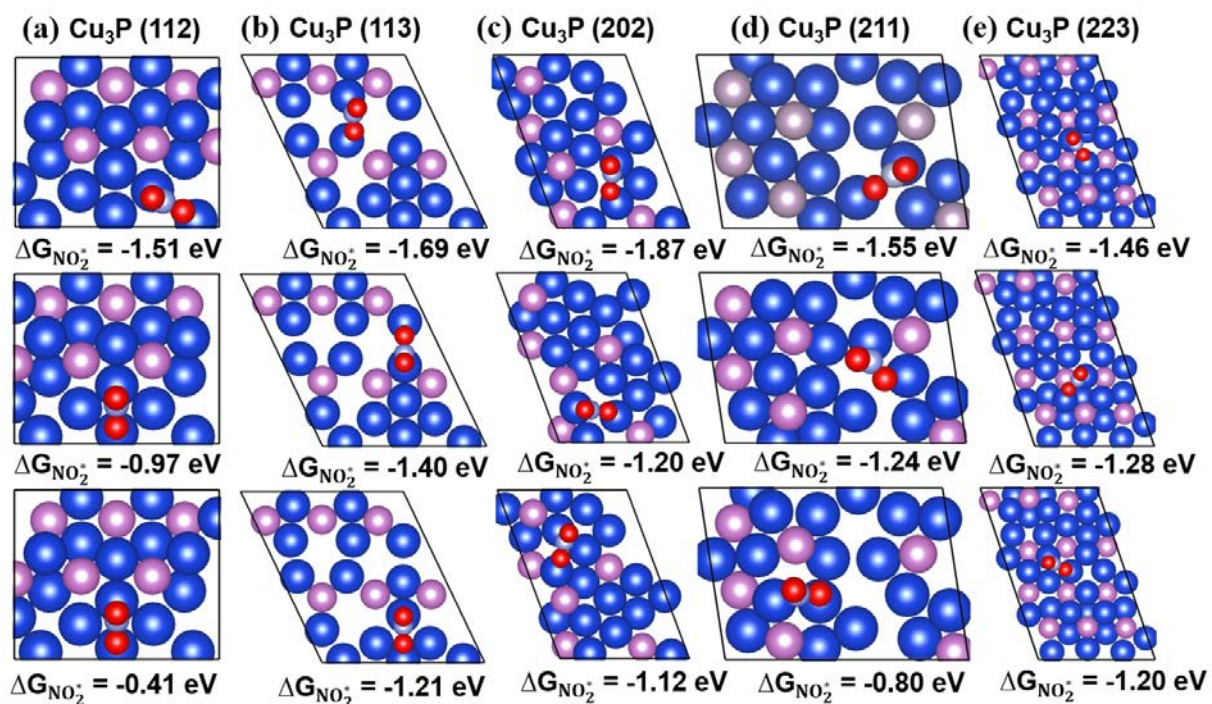


**Fig. S26.** The atomic structures together with the adsorption free energies for the three configurations with higher stability are given for NO<sub>2</sub><sup>-</sup> adsorption on the Cu<sub>3</sub>P(112), (113), (202), (211), and (223) surfaces.

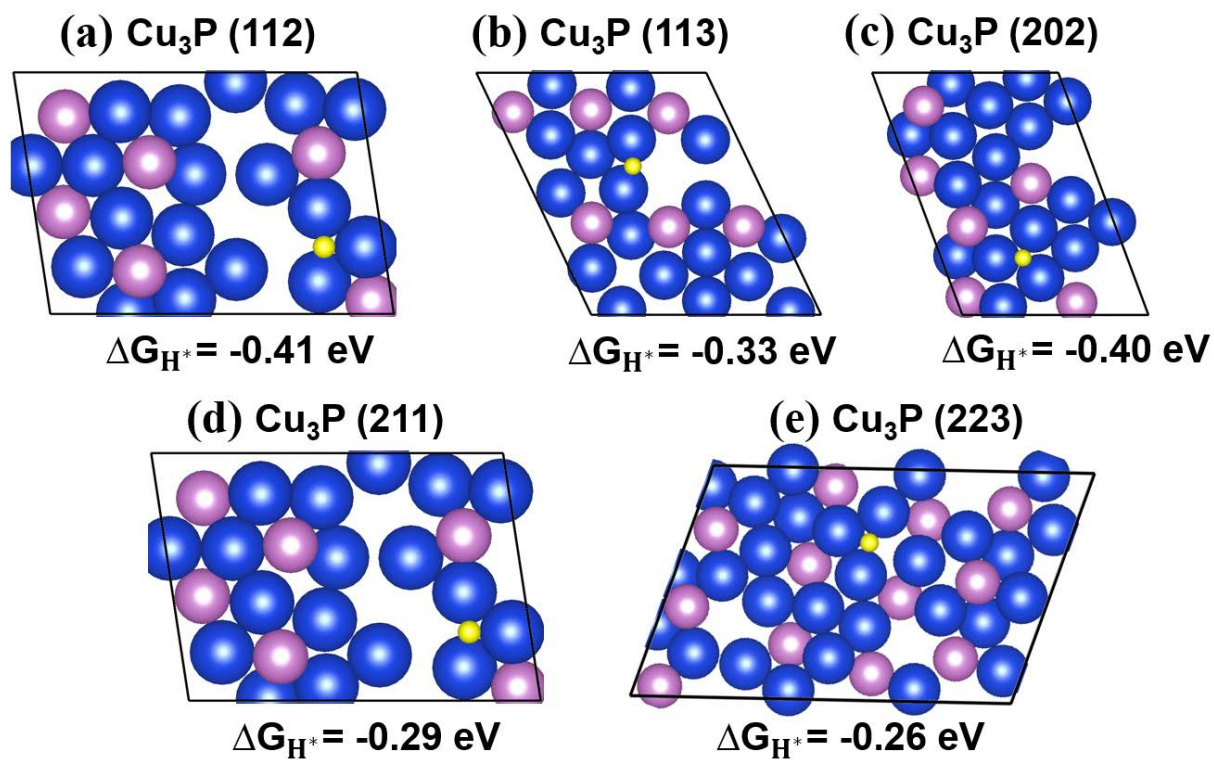


**Fig. S27.** The atomic structures together with the adsorption free energies for the atomic H adsorption on the  $\text{Cu}_3\text{P}$ (112), (113), (202), (211), and (223) surfaces.

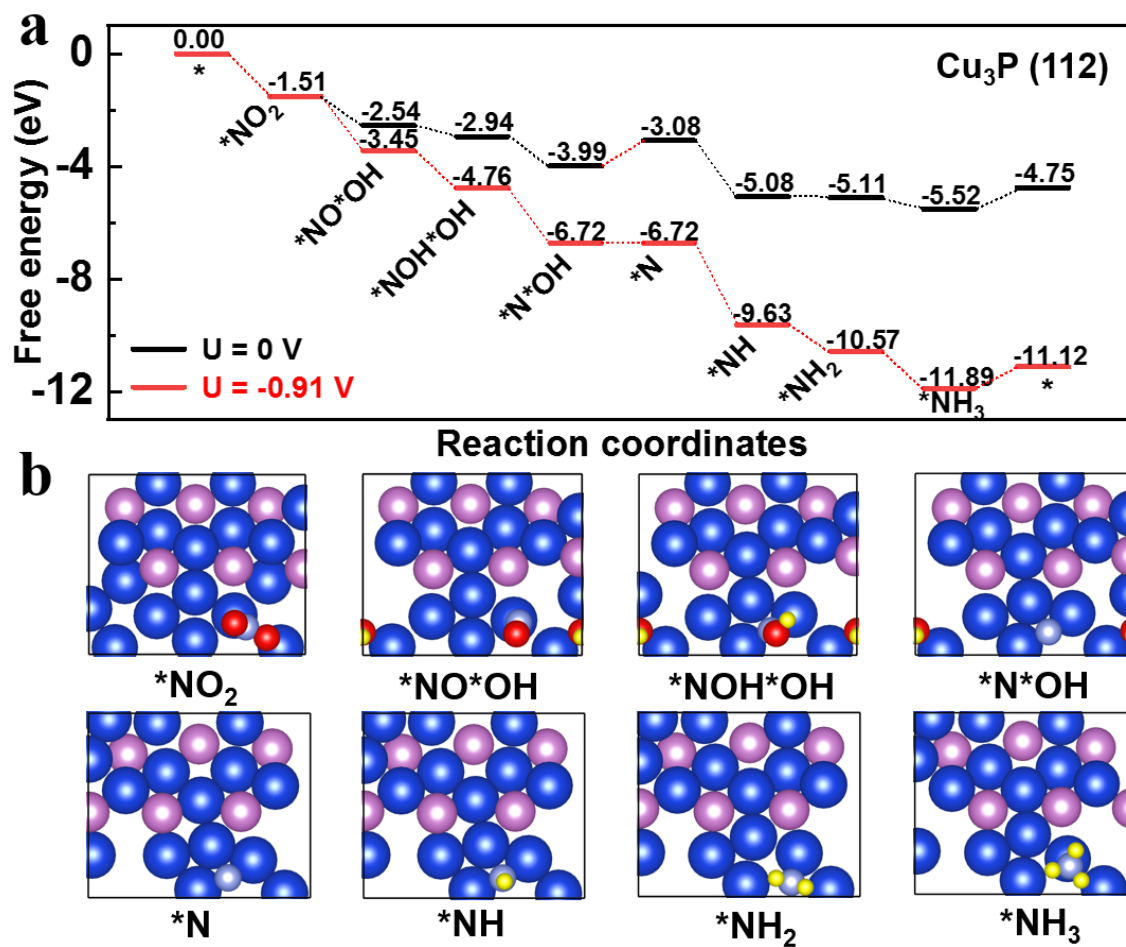


**Fig. S28.** (a) Free energy diagrams at different applied potentials for the nitrite reduction process on the  $\text{Cu}_3\text{P}(112)$  surface. (b) Atomic structures of the corresponding intermediates.

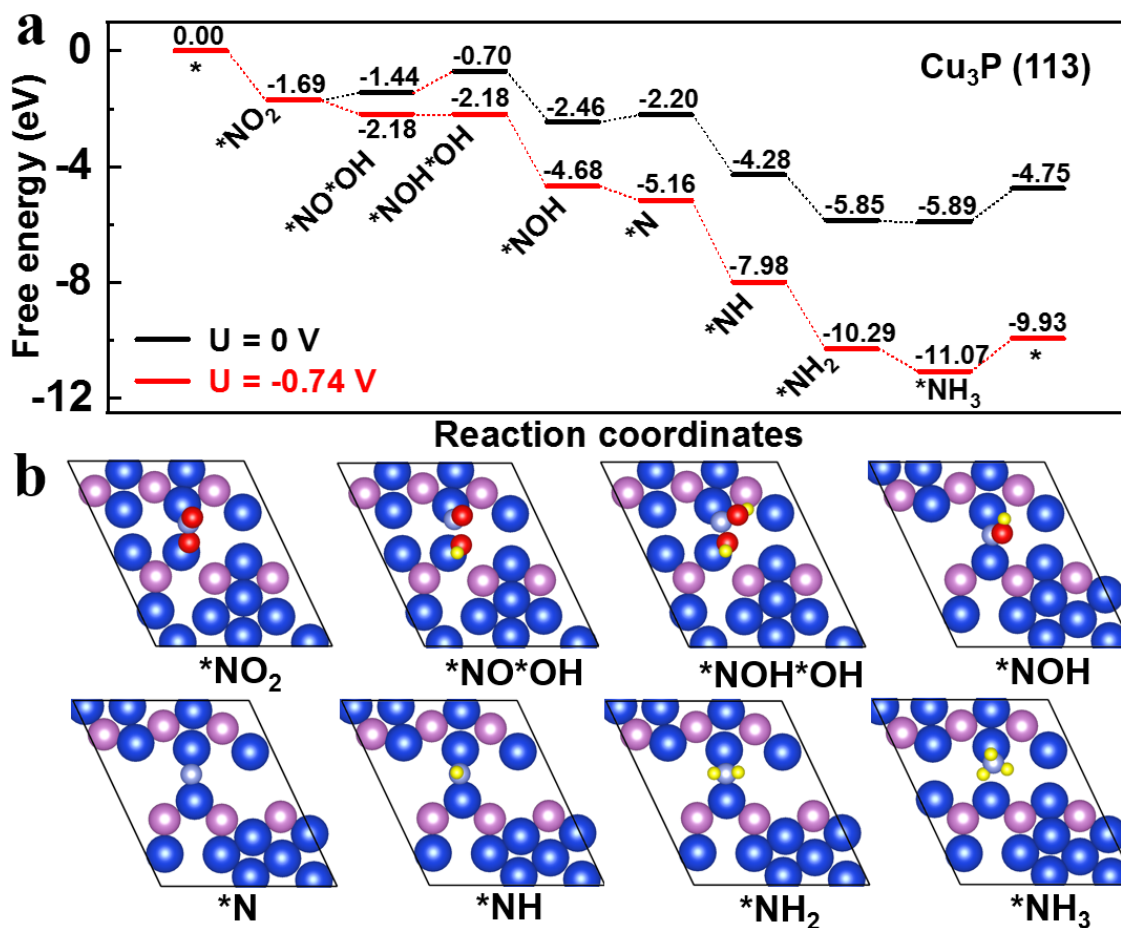


**Fig. S29.** (a) Free energy diagrams at different applied potentials for the nitrite reduction process on the Cu<sub>3</sub>P(113) surface. (b) Atomic structures of the corresponding intermediates.

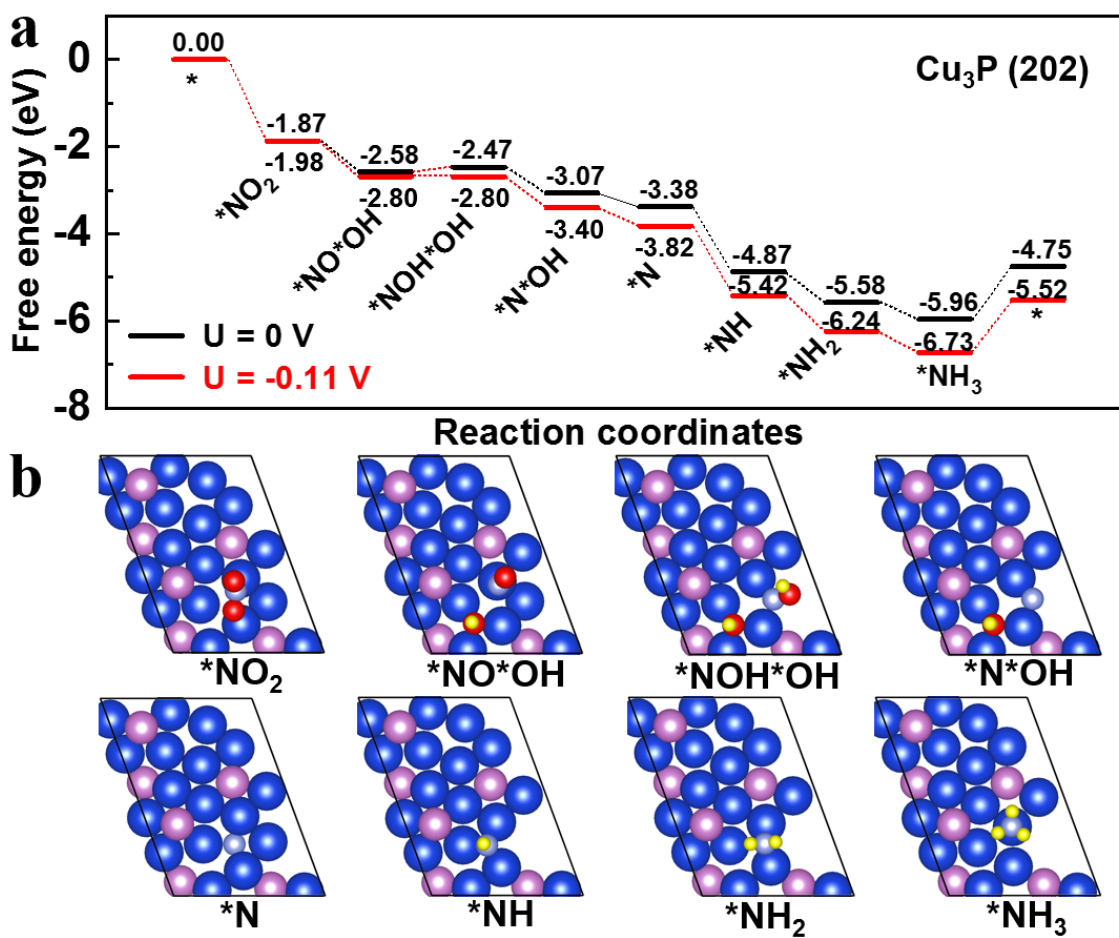


**Fig. S30.** (a) Free energy diagrams at different applied potentials for the nitrite reduction process on the  $\text{Cu}_3\text{P}(202)$  surface. (b) Atomic structures of the corresponding intermediates.

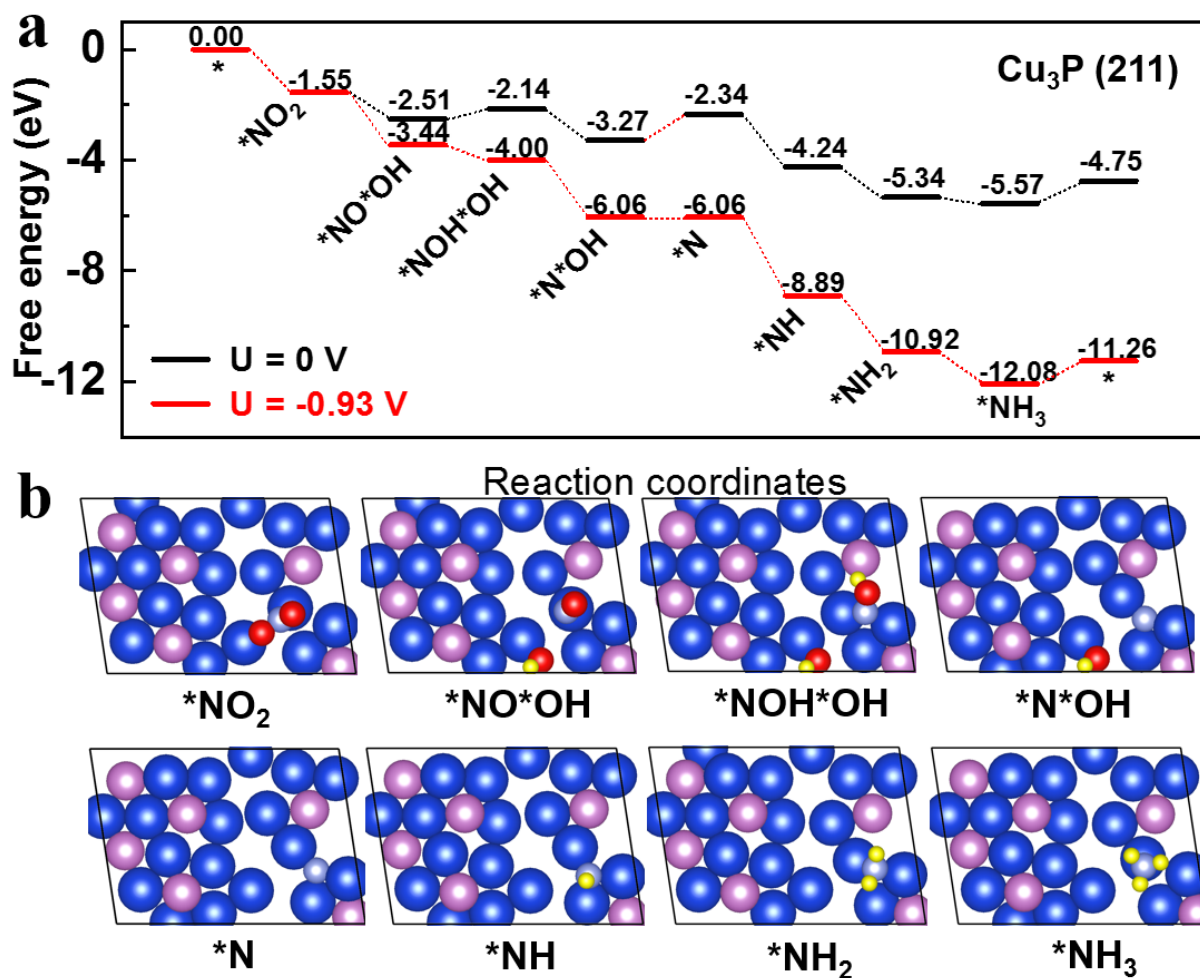


**Fig. S31.** (a) Free energy diagrams at different applied potentials for the nitrite reduction process on the  $\text{Cu}_3\text{P(211)}$  surface. (b) Atomic structures of the corresponding intermediates.

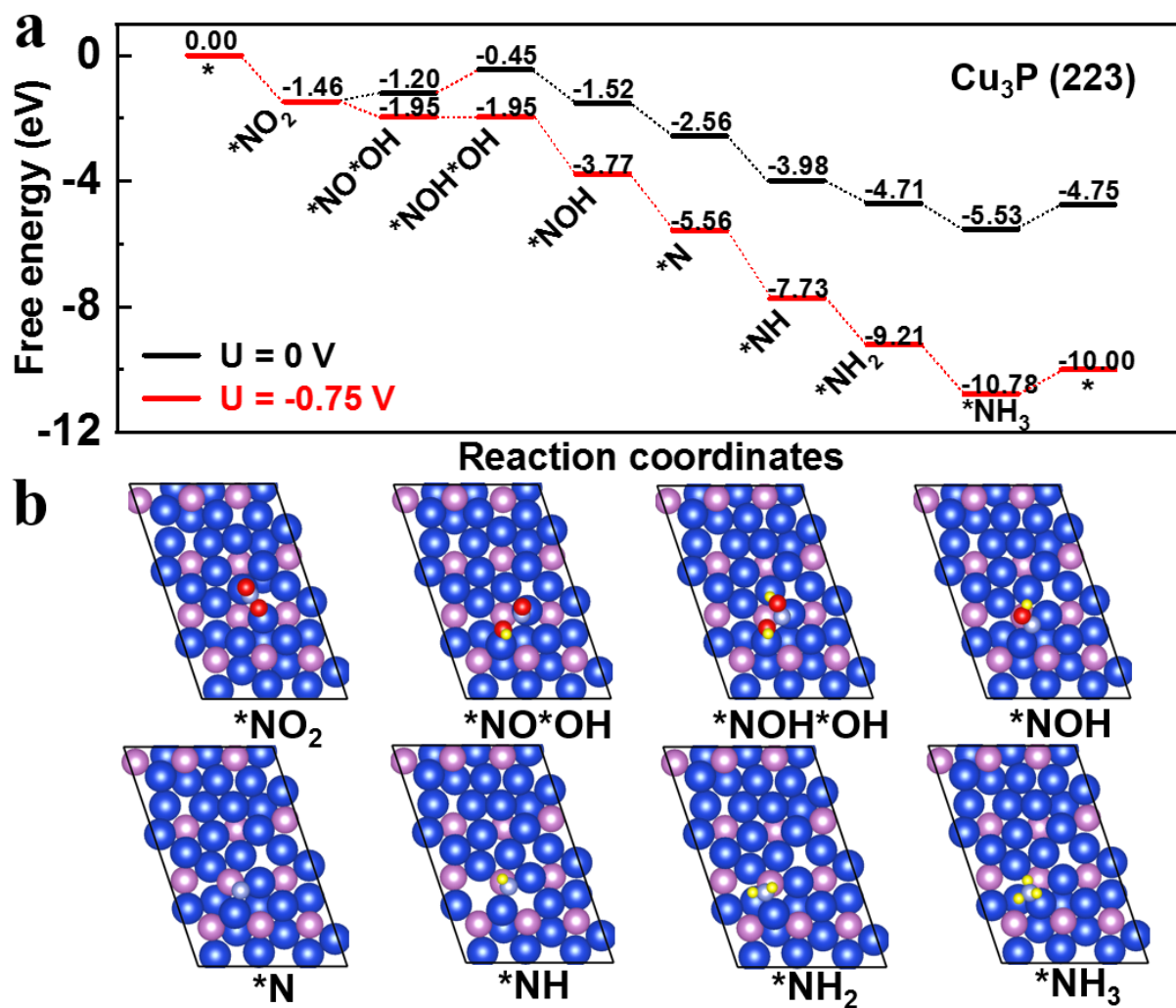


**Fig. S32.** (a) Free energy diagrams at different applied potentials for the nitrite reduction process on the  $\text{Cu}_3\text{P}(223)$  surface. (b) Atomic structures of the corresponding intermediates.

**Table S1.** Performance comparison of Cu<sub>3</sub>P NA/CF with other NO<sub>2</sub><sup>-</sup>RR electrocatalysts under ambient conditions.

Catalyst	Electrolyte	NH <sub>4</sub> <sup>+</sup> /NH <sub>3</sub> yield rate	FE (%)	Selectivity(%)	Ref.
Cu <sub>3</sub> P NA/CF	0.1 M PBS (0.1 M NO <sub>2</sub> <sup>-</sup> )	1626.6 ± 36.1 μg h <sup>-1</sup> cm <sup>-2</sup>	91.2 ± 2.5	88 ± 1.6	This work
Ni-NSA-V <sub>Ni</sub>	0.2 M Na <sub>2</sub> SO <sub>4</sub> (200 ppm NaNO <sub>2</sub> )	235.98 μmol h <sup>-1</sup> cm <sup>-2</sup>	88.9	77.2	14
MnO <sub>2</sub> nanoarrays	0.1 M Na <sub>2</sub> SO <sub>4</sub> (NaNO <sub>2</sub> )	3.09 × 10 <sup>-11</sup> mol s <sup>-1</sup> cm <sup>-2</sup>	6	-	15
Cobalt-tripeptide complex	1.0 M MOPS (1.0 M NaNO <sub>2</sub> )	3.01 × 10 <sup>-10</sup> mol s <sup>-1</sup> cm <sup>-2</sup>	90 ± 3	-	16
Poly-NiTRP complex	0.1 M NaClO <sub>4</sub> (NaNO <sub>2</sub> )	1.1 mM	-	-	17
Cu phthalocyanine complexes	0.1 M KOH (NaNO <sub>2</sub> )	-	78	-	18
[Co(DIM)Br <sub>2</sub> ] <sup>+</sup> (Carbon rod working electrode)	0.1 M solution of NaNO <sub>2</sub>	-	88	-	19
Oxo-MoS <sub>x</sub>	0.1 M nitrite in 0.2 M citric acid (pH = 5)	-	13.5	-	20
GCC-CoDIM	0.5 M Na <sub>2</sub> SO <sub>4</sub> with 20 mM NaNO <sub>2</sub>	-	99.5	-	21
Cu <sub>x</sub> Ir <sub>1-x</sub>	0.1 M phosphate buffer (100 ppm)	-	-	~100%	22
Rh/Al <sub>2</sub> O <sub>3</sub>	25 mM phosphate buffer (50 mM NO <sub>2</sub> <sup>-</sup> )	-	-	~68–95%	23
FeN <sub>5</sub> H <sub>2</sub>	1.0 M MOPS and 1.0 M NaNO <sub>2</sub>	-	-	> 90%	24
Cu <sub>80</sub> Ni <sub>20</sub>	1.0 M NaOH (20 mM NaNO <sub>2</sub> )	-	87.6	96	25

**Table S2.** Performance comparison of Cu<sub>3</sub>P NA/CF with other NO<sub>3</sub><sup>-</sup>RR electrocatalysts under ambient conditions.

Catalyst	Electrolyte	NH <sub>4</sub> <sup>+</sup> /NH <sub>3</sub> yield rate	FE (%)	Ref.
Cu <sub>3</sub> P NA/CF	0.1 M NO <sub>2</sub> <sup>-</sup> (0.1 M PBS)	848.7 ± 18.0 μg h <sup>-1</sup> cm <sup>-2</sup>	62.9 ± 2.0%	This work
Cu nanosheets	0.1 M KOH	390.1 μg h <sup>-1</sup> mg <sup>-1</sup>	99.7	26
PTCDA/O-Cu	0.1 M PBS (500 ppm NO <sub>3</sub> <sup>-</sup> )	436 ± 85 μg h <sup>-1</sup> cm <sup>-2</sup>	85.9	27
Pd-In/c-Al <sub>2</sub> O <sub>3</sub>	3.28 mM NaHCO <sub>3</sub> with nitrate-reservoir	-	71.5	28
Co <sub>3</sub> O <sub>4</sub> @NiO HNTs	0.5 M Na <sub>2</sub> SO <sub>4</sub> (200 ppm NO <sub>3</sub> <sup>-</sup> )	6.93 mmol h <sup>-1</sup> g <sup>-1</sup>	54.97	29
NiPc complex	0.1 M KOH, in the presence of NO <sub>3</sub> <sup>-</sup>	-	85	30
Cu	1 M NaOH (0.1 M NaNO <sub>3</sub> )	-	79	31
Cu <sub>50</sub> Ni <sub>50</sub>	1 M KOH (10 mM KNO <sub>3</sub> )	-	84 ± 2	32
Ti/GC	KOH (~0.1 to 0.6 M NO <sub>3</sub> <sup>-</sup> )	-	82	33
NTEs	NaCl (0.65 mM NaNO <sub>3</sub> )	-	5.6	34

**Table S3.** Comparison of  $\text{NH}_4^+$  ( $\text{NH}_3$ ) yield rate for electrocatalytic  $\text{Cu}_3\text{P}$  NA/CF with other NRR electrocatalysts under ambient conditions.

Catalyst	Reaction	$\text{NH}_4^+/\text{NH}_3$ yield rate	Ref.
$\text{Cu}_3\text{P}$ NA/CF	$\text{NO}_2^-$ RR	$1626.6 \pm 36.1 \mu\text{g h}^{-1} \text{cm}^{-2}$	This work
	$\text{NO}_3^-$ RR	$848.7 \pm 18.0 \mu\text{g h}^{-1} \text{cm}^{-2}$	This work
$\text{Mo}_3\text{Si}$	NRR	$12.24 \times 10^{-10} \mu\text{g h}^{-1} \text{cm}^{-2}$	35
$\text{MoO}_3$	NRR	$4.80 \times 10^{-10} \text{mol h}^{-1} \text{cm}^{-2}$	36
Bi nanosheet array	NRR	$6.89 \times 10^{-11} \text{mol h}^{-1} \text{cm}^{-2}$	37
$\text{Ti}^{3+}$ - $\text{TiO}_{2-x}$	NRR	$3.51 \times 10^{-11} \text{mol h}^{-1} \text{cm}^{-2}$	38
$\text{TiB}_2/\text{GP}$	NRR	$1.75 \times 10^{-10} \text{mol s}^{-1} \text{cm}^{-2}$	39
$\text{C}@\text{CoS}@\text{TiO}_2$	NRR	$8.09 \times 10^{-10} \text{mol s}^{-1} \text{cm}^{-2}$	40
$\text{CrO}_{0.66}\text{N}_{0.56}$	NRR	$8.9 \times 10^{-11} \text{mol s}^{-1} \text{cm}^{-2}$	41
$\text{CuO}/\text{graphene}$	NRR	$1.8 \times 10^{-10} \text{mol s}^{-1} \text{cm}^{-2}$	42
$\text{Ti}/\text{Fe}_3\text{O}_4$	NRR	$5.6 \times 10^{-11} \text{mol s}^{-1} \text{cm}^{-2}$	43

**Table S4.** The calculated zero-point energy ( $E_{\text{ZPE}}$ ) and the product ( $TS$ ) of temperature ( $T = 298.15$  K) and entropy ( $S$ ) of the different species along the reaction pathway presented in Fig. 5a, where \* represents the adsorption site.

Species	$E_{\text{ZPE}}$ (eV)	$TS$ (eV)
*NO <sub>2</sub>	0.28	0.23
*NO*OH	0.50	0.29
*NO	0.18	0.14
*NOH	0.47	0.14
*NHOH	0.80	0.16
*NH	0.39	0.04
*NH <sub>2</sub>	0.71	0.08
*NH <sub>3</sub>	1.03	0.15

**Table S5.** Similar to Table S4, except that it is for the he reaction pathway presented in Fig. S21.

Species	$E_{\text{ZPE}}$ (eV)	$TS$ (eV)
*NO <sub>2</sub>	0.27	0.28
*NO*OH	0.52	0.23
*NO	0.16	0.15
*NOH	0.47	0.13
*NHOH	0.08	0.03
*NH	0.39	0.04
*NH <sub>2</sub>	0.70	0.08
*NH <sub>3</sub>	1.03	0.15

## References

- 1 D. Zhu, L. Zhang, R. E. Ruther and R. J. Hamers, *Nat. Mater.*, 2013, **12**, 836–841.
- 2 L. C. Green *Anal. Biochem.*, 1982, **126**, 131–138.
- 3 G. W. Watt and J. D. Chrisp, *Anal. Chem.*, 1952, **24**, 2006–2008.
- 4 G. Kresse and J. Furthmüller, *Set. Phys. Rev. B*, 1996, **54**, 11169–11186.
- 5 P. E. Blöchl, *Phys. Rev. B*, 1994, **50**, 17953–17979.
- 6 J. P. Perdew, K. Burke and M. Ernzerhof, *Phys. Rev. Lett.*, 1996, **77**, 3865–3868.
- 7 S. Grimme, J. Antony, S. Ehrlich and H. Krieg, *J. Chem. Phys.*, 2010, **132**, 154104.
- 8 G. Henkelman, A. Arnaldsson and H. Jónsson, *Comput. Mater. Sci.*, 2006, **36**, 354–360.
- 9 H. J. Monkhorst and J. D. Pack, *Phys. Rev. B*, 1976, **13**, 5188–5192.
- 10 I. Mondal, A. Mahata, H. Kim, U. Pal, F. De Angelis and J. Y. Park, *Nanoscale*, 2020, **12**, 17769–17779.
- 11 J. K. Nørskov, J. Rossmeisl, A. Logadottir, L. Lindqvist, J. R. nKitchin, T. Bligaard and H. Jónsson, *J. Phys. Chem. B*, 2004, **108**, 17886–17892.
- 12 <http://webbook.nist.gov/chemistry/>.
- 13 S. Guo, K. Heck, S. Kasiraju, H. Qian, Z. Zhao, L. C. Grabow, J. T. Miller and M. S. Wong, *ACS Catal.*, 2018, **8**, 503–515.
- 14 C. H. Wang, W. Zhou, Z. J. Sun, Y. T. Wang, B. Zhang and Y. F. Yu, *J. Mater. Chem. A*, 2021, **9**, 239–243.
- 15 R. Wang, Z. Wang, X. Xiang, R. Zhang, X. Shi and X. Sun, *Chem. Commun.*, 2018, **54**, 10340–10342.
- 16 Y. Guo, J. R. Stroka, B. Kandemir, C. E. Dickerson and K. L. Bren, *J. Am. Chem. Soc.*, 2018, **140**, 16888–16892.
- 17 P. Dreyse, M. Isaacs, K. Calfumán, C. Cáceres, A. Aliaga, M. J. Aguirre and D. Villagra, *Electrochim. Acta*, 2011, **56**, 5230–5237.
- 18 N. Chebotareva and T. Nyokong, *J. Appl. Electrochem.*, 1997, **27**, 975–981.
- 19 S. Xu, H. Y. Kwon, D. C. Ashley, C. H. Chen, E. Jakubikova and J. M. Smith, *Inorg. Chem.*, 2019, **58**, 9443–9451.
- 20 D. He, Y. Li, H. Ooka, Y. K. Go, F. Jin, S. H. Kim and R. Nakamura, *J. Am. Chem. Soc.*, 2018, **140**, 2012–2015.
- 21 S. E. Braley, J. Xie, Y. Losovyj and J. M. Smith, *J. Am. Chem. Soc.*, 2021, DOI: 10.1021/jacs.1c03427.
- 22 H. Li, C. X. Yan, H. Y. Guo, K. Y. Shin, S. M. Humphrey, C. J. Werth and G. Henkelman,

- ACS Catal.*, 2020, **10**, 7915–7921.
- 23 C. A. Clark, C. P. Reddy, H. Xu, K. N. Heck, G. Luo and T. P. Senftle, *ACS Catal.*, 2020, **10**, 494–509.
- 24 J. R. Stroka, B. Kandemir, E. M. Matson and K. L. Bren, *ACS Catal.*, 2020, **10**, 13968–13972.
- 25 L. Mattarozzi, S. Cattarin, N. Comisso, P. Guerriero, Marco Musiani, L. Vázquez-Gómez and E. Verlato, *Electrochim. Acta*, 2013, **89**, 488–496.
- 26 X. Fu, X. Zhao, X. Hu, K. He, Y. Yu, T. Li, Q. Tu, X. Qian, Q. Yue, M. R. Wasielewski and Y. Kang, *Y. Appl. Mater. Today*, 2020, **19**, 100620.
- 27 G.-F. Chen, Y. Yuan, H. Jiang, S.-Y. Ren, L.-X. Ding, L. Ma, T. Wu, J. Lu and H. Wang, *Nat. Energy*, 2020, **5**, 605–613.
- 28 B. P. Chaplin, J. R. Shapley and C. J. Werth, *Catal. Lett.*, 2009, **130**, 56–62.
- 29 Y. Wang, C. Liu, B. Zhang and Y. Yu, *Sci. China Mater.*, 2020, **63**, 2530–2538.
- 30 N. Chebotareva and T. Nyokong, *J. Appl. Electrochem.*, 1997, **27**, 975–981.
- 31 D. Reyter, G. Chamoulaud, D. Bélanger and L. Roué, *J. Electroanal. Chem.*, 2006, **596**, 13–24.
- 32 Y. Wang, A. Xu, Z. Wang, L. Huang, J. Li, F. Li, J. Wicks, M. Luo, D.-H. Nam, C.-S. Tan, Y. Ding, J. Wu, Y. Lum, C.-T. Dinh, D. Sinton, G. Zheng and E. H. Sargent, *J. Am. Chem. Soc.*, 2020, **142**, 5702–5708.
- 33 J. M. McEnaney, S. J. Blair, A. C. Nielander, J. A. Schwalbe, D. M. Koshy, M. Cargnello and T. F. Jaramillo, *ACS Sustainable Chem. Eng.*, 2020, **8**, 2672–2681.
- 34 X. Ma, M. Li, C. Feng, W. Hu, L. Wang and X. Liu, *J. Electroanal. Chem.*, 2016, **782**, 270–277.
- 35 T. Wang, Q. Liu, T. Li, S. Lu, G. Chen, X. Shi, A. M. Asiri, Y. Luo, D. Ma and X. Sun, *J. Mater. Chem. A*, 2021, **9**, 884–888.
- 36 J. Han, X. Ji, X. Ren, G. Cui, L. Li, F. Xie, H. Wang, B. Li and X. Sun, *J. Mater. Chem. A*, 2018, **6**, 12974.
- 37 R. Zhang, L. Ji, W. Kong, H. Wang, R. Zhao, H. Chen, T. Li, B. Li, Y. Luo and X. Sun, *Chem. Commun.*, 2019, **55**, 5263–5266.
- 38 B. Li, X. Zhu, J. Wang, R. Xing, Q. Liu, X. Shi, Y. Luo, S. Liu, X. Niu and X. Sun, *Chem. Commun.*, 2020, **56**, 1074–1077.
- 39 S. Li, Y. Wang, J. Liang, T. Xu, D. Ma, Q. Liu, T. Li, S. Xu, G. Chen, A. M. Asiri, Y. Luo, Q. Wu and X. Sun, *Mater. Today Phys.*, 2021, **18**, 100396.
- 40 Y. Liu, X. Chen, J. Yu and B. Ding, Carbon-nanoplated CoS@TiO<sub>2</sub> nanofibrous

- membrane: an interface-engineered heterojunction for high-efficiency electrocatalytic nitrogen reduction, *Angew. Chem. Int. Ed.*, 2019, **58**, 18903–18907.
- 41 Y. Yao, Q. Feng, S. Zhu, J. Li, Y. Yao, Y. Wang, Q. Wang, M. Gu, H. Wang, H. Li, X. Yuan and M. Shao, Chromium oxynitride electrocatalysts for electrochemical synthesis of ammonia under ambient conditions, *Small Methods*, 2019, **3**, 1800324.
- 42 F. Wang, Y. Liu, H. Zhang and K. Chu, CuO/graphene nanocomposite for nitrogen reduction reaction, *ChemCatChem*, 2019, **11**, 1441–1447.
- 43 Q. Liu, X. Zhang, B. Zhang, Y. Luo, G. Cui, F. Xie and X. Sun, Ambient N<sub>2</sub> fixation to NH<sub>3</sub> electrocatalyzed by a spinel Fe<sub>3</sub>O<sub>4</sub> nanorod, *Nanoscale*, 2018, **10**, 14386–14389.